DOI: 10.13009/EUCASS2025-594
11TH EUROPEAN CONFERENCE FOR AERONAUTICS AND SPACE SCIENCES (EUCASS)

Cislunar Optical Track-to-Track Correlation with an Optimal Control-based Approach

Alessia De Riz⋆†, *Riccardo Cipollone*⋆, *Pierluigi Di Lizia* ⋆
⋆*Department of Aerospace Science and Technology, Politecnico Di Milano*
Via Giuseppe La Masa 32, Milan, 20156, Lombardy, Italy
†alessia.deriz@polimi.it · riccardo.cipollone@polimi.it · pierluigi.dilizia@polimi.it
†Corresponding author

Abstract

The growing interest in cislunar space have heightened the need for advanced Space Situational Awareness (SSA) and Space Surveillance and Tracking (SST) capabilities. This work explores the cislunar application of a novel method for track-to-track correlation using optical data and a minimum-energy optimal control problem (OCP), a promising approach due to its minimal assumptions on orbital dynamics. The method involves correlating two optical uncorrelated tracks (UCTs), represented as attributables, which define the boundary conditions of the OCP. Solved using an indirect approach with single shooting, the OCP minimizes thrust energy under a reference dynamics model. Uncertainty in boundary conditions is propagated through the process to evaluate solution distributions, which are used to derive correlation scores. A cislunar Initial Orbit Determination (IOD) method, extending the Two-Body Integral method to the Circular Restricted Three-Body Problem (CR3BP), provides initial state estimates. Performance is assessed through numerical tests employing synthetic ground and space-based optical measurements of three-body targets, sensor accuracy is also included to model uncertainty. Results demonstrate the potential of the developed approach for future cislunar SST applications.

1. Introduction

In recent years, the cislunar environment, a relatively unexplored region of space between the Earth and the Moon, has attracted growing attention from both public and private stakeholders. This interest is motivated by long-term objectives in deep space exploration, planned lunar infrastructure, and the potential exploitation of in situ resources. As mission activity in this domain intensifies, there is a pressing need to develop tailored Space Situational Awareness (SSA) and Space Traffic Management (STM) capabilities to ensure long-term sustainability.
Unlike near-Earth space, the cislunar region presents unique challenges due to its larger spatial scale, more complex gravitational dynamics, and limited observational infrastructure. In this context, maintaining and updating objects catalogue, tracking both active and inactive assets, will be key to preventing potential congestion and collision risks in this newly active orbital domain.[6]

As part of the cataloguing pipeline, track-to-track correlation or association plays a critical role when a new Resident Space Object (RSO) is detected and needs to be integrated into the catalogue. At the core of this process lies the concept of track, which denotes a series of consecutive observations of the same target taken by a single sensor within a restrained timeframe, usually insufficient to estimate a reliable orbit. When it comes to measurement processing, an acquired track is typically labelled as an Uncorrelated Track (UCT) until it can be matched with a catalogued object that is confirmed to have generated it.

In the framework of extending SST techniques to the cislunar environment, numerous developments have emerged aimed at adapting well-established two-body dynamics approaches to this more complex setting. Among these, the Admissible Region (AR) concept has seen various potential applications. For instance, Wisnek[15] and Bolden[2] utilize different types of constraints to limit the search space, incorporating sensor characteristics and visibility constraints between the observer and potential targets. Another example is found in Liu[7] with the CR3BP-DAIOD method, where the AR is defined based on threshold values of range, range rate, Jacobi constant, and orbital energy relative to Earth for each major family of cislunar orbits. Other methods have also been devised as in Liu[8] where the number of possible IOD solutions derived from the perturbed-Laplace (PL) method, conceptually similar to the classical Laplace method but adapted for three-body dynamics, are assessed. Additionally, Liu[7] introduces alternative approaches beyond the AR, including Earth-centered and Moon-centered Gauss methods, to estimate missing range values. These initial

DOI: 10.13009/EUCASS2025-594

guesses are essential when processing three optical observations to solve two third-body-perturbed Lambert problems, ultimately yielding the CR3BP trajectory that best fits the data.

However, these approaches often rely on multiple assumptions about the observed objects dynamics. To overcome such limitations, alternative techniques emerge such as the use of Physics-Informed Neural Networks (PINNs) in Scorsoglio,[12] where the orbit determination problem is framed dynamically, aiming to solve the governing differential equations directly from observational data.

Another promising approach that avoids strong a priori assumptions is based on control distance metrics. This concept was first introduced by Holzinger,[5] who developed a technique to estimate the minimum control effort required to match an observation, using control-based metrics instead of the more conventional Mahalanobis distance. This foundational idea laid the groundwork for subsequent studies, such as Pastor,[10] which extended the approach to impulsive manoeuvre detection and correlation. To narrow the search space during the minimisation of these metrics, the method is often combined with admissible region constraints, as demonstrated in the works of Serra[13] and Siminski.[14] Given the flexibility, minimal assumptions, and sensitivity to manoeuvres of this approach, it appears well-suited for investigation in a cislunar context.

This work extends a methodology, previously introduced for near-Earth applications[3] to the cislunar domain, employing an energy-based optimal control metric shaped by transversality conditions to replace the need for a predefined admissible region. The approach enables the association of tracks consistent with ballistic motion while remaining robust to manoeuvres, an essential feature for effective cislunar catalogue maintenance, where dynamic diversity and sparse observations increase the risk of object duplication.

2. Methodology

This section presents the core methodology and its main components. Beginning with a brief overview of the dynamical model leveraged in the analyses, followed by the formulation of the minimum-energy Optimal Control Problem (OCP) tailored to the specific application. Finally, the workflow detailing how uncertainty is integrated and propagated throughout the pipeline is outlined.

2.1 Circular Restricted Three-Body Problem

The Circular Restricted Three-Body Problem (CR3BP) provides a reliable model for cislunar orbital dynamics, particularly when the Moon's gravitational influence is too significant to be treated as a mere perturbation to Earth-centered Keplerian motion. While the two-body problem suffices near a single dominant mass like Earth, in cislunar space the Moon's mass and distance necessitate a more accurate model.

The CR3BP considers a third body of negligible mass (e.g., a spacecraft) moving under the gravitational influence of two massive bodies, Earth (primary) and Moon (secondary) and orbiting their common barycenter in circular, coplanar orbits. This model assumes the third body does not affect the motion of the primaries. A synodic reference frame, centered at the barycenter and rotating with the primaries, is typically used to simplify analysis. The x-axis aligns with the Earth-Moon line, the z-axis is normal to the orbital plane, and the y-axis completes the right-handed system as illustrated in Fig. 1.

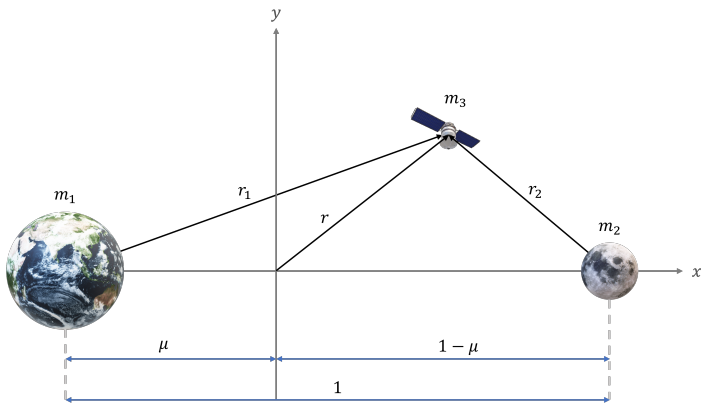

Figure 1: Synodic frame.

In the non-dimensional form of the CR3BP, the total mass of the system, the Earth-Moon distance, and the

DOI: 10.13009/EUCASS2025-594

angular velocity of the rotating frame are normalized to 1. Let μ be the mass ratio of the Moon, with the Earth and Moon positioned at $(-\mu, 0)$ and $(1-\mu, 0)$, respectively. The equations of motion in the rotating frame are:

$$\ddot{x} - 2\dot{y} = \frac{\partial \Omega}{\partial x},\ \ddot{y} + 2\dot{x} = \frac{\partial \Omega}{\partial y},\ \ddot{z} = \frac{\partial \Omega}{\partial z}, \tag{1}$$

where the pseudo-potential function $\Omega(x, y, z)$ is defined as:

$$\Omega(x, y, z) = \frac{1}{2}(x^2 + y^2) + \frac{1-\mu}{r_1} + \frac{\mu}{r_2},$$

and r_1 and r_2 are the distances from the third body to the Earth and Moon, respectively, given by:

$$r_1 = \sqrt{(x+\mu)^2 + y^2 + z^2}, \quad r_2 = \sqrt{(x-1+\mu)^2 + y^2 + z^2}.$$

The system admits five equilibrium points, called Lagrange points, where the net acceleration in the rotating frame is zero. Three of them L_1, L_2, and L_3 lie along the Earth-Moon line and are collinear with the primaries, while the other two L_4 and L_5 form equilateral triangles with the primaries. These points are crucial for mission design due to their dynamic and gravitational properties.

2.2 Minimum-energy Optimal Control Problem framework with Transversality Conditions

The developed technique aims at solving a correlation problem between two optical Uncorrelated Tracks (UCTs), where the only available information consists of the target's angular coordinates, Right Ascension (α) and Declination (δ), contained within the UCT itself. These angular pairs also serve as the boundary conditions (BCs) for the problem. Optical sensors are chosen over radar due to their higher suitability for future space-based SST applications in the cislunar domain.
To estimate the target's state in an Earth-Centered Inertial (ECI) reference frame, the following relationships are generally employed:

$$\begin{aligned} \mathbf{r} &= \mathbf{R_o} + \rho \mathbf{s}, \\ \mathbf{v} &= \mathbf{V_o} + \rho \dot{\mathbf{s}} + \dot{\rho} \mathbf{s}, \\ \mathbf{s} &= (\cos\alpha \cos\delta, \sin\alpha \cos\delta, \sin\delta), \end{aligned} \tag{2}$$

where $\mathbf{r}$ and $\mathbf{v}$ represent the target's position and velocity, while $\mathbf{R_o}$ and $\mathbf{V_o}$ are the observer's position and velocity, and $\mathbf{s}$ is the line-of-sight unit vector. However, angular information alone is not sufficient for state determination. To overcome this, a track compression technique is used to extract angular velocity information $(\dot{\alpha}, \dot{\delta})$ through a second-order regression applied at the midpoint of the UCT. This condenses the track into a single point, resulting in the so-called attributable vector $\mathbf{a} = [\alpha,\ \delta,\ \dot{\alpha},\ \dot{\delta}]$.[9]

To link two attributables, an energy-optimal control problem is formulated, minimizing the total thrust energy:

$$J = \frac{1}{2} \int_{t_0}^{t_f} \mathbf{u}(\tau)^T \mathbf{u}(\tau)\, d\tau\ ,$$

where $\mathbf{u}(t)$ is the acceleration (control) profile, and t_0, t_f denote the initial and final times. This assumption of minimum-energy optimality is justified both by the natural objective to minimize fuel and by the fact that true target motion is typically close to ballistic. The OCP is formulated as follows:

$$\min_{\mathbf{u}(\tau)} J = \int_{t_0}^{t_f} \frac{1}{2} \mathbf{u}(\tau)^T \mathbf{u}(\tau)\, d\tau \quad \text{s.t.} \quad \begin{cases} \dot{\mathbf{x}} = \mathbf{f}(t, \mathbf{x}(t), \mathbf{u}(t)) \\ \mathbf{h}(\mathbf{x}(\mathrm{t_0})) = \mathbf{a}_0 \\ \mathbf{h}(\mathbf{x}(\mathrm{t_f})) = \mathbf{a}_f \\ t_0, t_f \text{ given}\ , \end{cases} \tag{3}$$

where $\mathbf{h}(\mathbf{x})$ transforms the synodic state into the attributable vector, and $\mathbf{x}(t_0)$, $\mathbf{x}(t_f)$ correspond to the initial and final synodic state vectors.

To solve the OCP of Eq. (3), an indirect method based on the Pontryagin Maximum Principle (PMP) is adopted. This approach transforms the problem into a Two-Point Boundary Value Problem (TPBVP) by augmenting the system state with the co-state vector $\boldsymbol{\lambda}$. From the necessary condition for optimality, the control input is derived by setting the partial derivative of the Hamiltonian $\mathcal{H}$ with respect to the control to zero, resulting in an optimal feedback law. The full system of equations defining the TPBVP consists of the state and co-state differential equations, along with the

DOI: 10.13009/EUCASS2025-594

boundary conditions, as reported in Eq. (4). The latter are enforced through the transformation from the synodic to ECI frame and then to spherical coordinates to retrieve the attributable vector at the initial and final times.

$$\mathcal{H} = \frac{1}{2}\mathbf{u}^T\mathbf{u} + \boldsymbol{\lambda_r}\cdot\mathbf{v} + \boldsymbol{\lambda_v}\cdot\left[\frac{\partial\Omega}{\partial x} + 2\dot{y},\ \frac{\partial\Omega}{\partial y} - 2\dot{x},\ \frac{\partial\Omega}{\partial z}\right] \quad \longrightarrow \quad \begin{cases}\dot{\mathbf{x}} = \mathcal{H}_\lambda \\ \dot{\boldsymbol{\lambda}} = -\mathcal{H}_x \\ \mathbf{h}(\mathbf{x}(\mathrm{t_0})) = \mathbf{a}_0 \\ \mathbf{h}(\mathbf{x}(\mathrm{t_f})) = \mathbf{a}_f\ .\end{cases} \tag{4}$$

Since the BCs only partially constrain the state, range and range rate are unknown from angular data, transversality conditions are leveraged instead of fixing $\mathbf{x}(t_0)$ or $\mathbf{x}(t_f)$ completely. These conditions, derived from PMP, connect the co-states and the BCs, yielding:

$$\boldsymbol{\lambda}_0 = -\frac{\partial V_0}{\partial \mathbf{x}_0}^T - \frac{\partial \mathbf{g}_0}{\partial \mathbf{x}_0}^T \boldsymbol{\nu_0}, \quad \boldsymbol{\lambda}_f = \frac{\partial V_f}{\partial \mathbf{x}_f}^T + \frac{\partial \mathbf{g}_f}{\partial \mathbf{x}_f}^T \boldsymbol{\nu_f} \quad ,$$

where $\boldsymbol{\nu_0}$ and $\boldsymbol{\nu_f}$ are Lagrange multipliers enforcing the constraints, and V_0, V_f are state cost functions, which in this case are set to zero. The constraint vectors $\mathbf{g}(\mathbf{x_0}, t_0)$, $\mathbf{g}(\mathbf{x_f}, t_f)$ encode the deviation between measured and computed attributables:

$$\mathbf{g}(\mathbf{x_0}, t_0) = \mathbf{a}_0(\mathbf{x}_0) - \overline{\mathbf{a}}_0, \quad \mathbf{g}(\mathbf{x_f}, t_f) = \mathbf{a}_f(\mathbf{x}_f) - \overline{\mathbf{a}}_f \quad ,$$

with the overlined terms representing the actual measurement data. This formulation allows one to retrieve analytical expressions for $\boldsymbol{\lambda}_0$ and $\boldsymbol{\lambda}_f$, leaving $\mathbf{x}_0$ and the multipliers $\boldsymbol{\nu}$ as unknowns. The full problem is solved iteratively via a single-shooting method, starting from an initial guess for both $\mathbf{x}_0$ and $[\boldsymbol{\nu_0}, \boldsymbol{\nu_f}]$. For this application the $\mathbf{x_0}$ used as a first guess for the iteration is derived from a devised cislunar IOD method, conceptually comparable to the Two-Body Integral method,[4] but revised for CR3BP applications. The detailed formulation of this approach is not included here, as it lies beyond the scope of the present study. The final nonlinear system comprises 14 equations in 14 unknowns:

$$\begin{cases} \boldsymbol{\lambda}(t_f) - \boldsymbol{\lambda_f} = 0 \\ \mathbf{g}(\mathbf{x_0}, t_0) = 0 \\ \mathbf{g}(\mathbf{x_f}, t_f) = 0\ , \end{cases} \tag{5}$$

where $\mathbf{x}(t_f)$ and $\boldsymbol{\lambda}(t_f)$ result from integrating the dynamics:

$$\mathbf{x}(t_f) = \boldsymbol{\phi}_x(t_f;\ \mathbf{x}_0,\ \boldsymbol{\lambda}_0,\ t_0), \quad \boldsymbol{\lambda}(t_f) = \boldsymbol{\phi}_\lambda(t_f;\ \mathbf{x}_0,\ \boldsymbol{\lambda}_0,\ t_0).$$

This comprehensive approach enables the reconstruction of optimal connecting trajectories and associated energy expenditures between UCTs using purely optical information.

2.3 Uncertainties and correlation

This section deals with how the uncertainty characterizing the angular measurements involved in the problem translates into the final results, generating distributions of solutions.

The first step is to derive the covariance relative to the whole attributable $\mathbf{a}$. The sensor accuracy is taken as standard deviation σ of α and δ measurements, thus describing the corresponding distribution, assumed Gaussian, by mean value and covariance. To propagate this uncertainty to the angular velocities, the process leverages an UT on the previously introduced track compression to retrieve mean and covariance of the whole corresponding attributable.

The underlying idea related to uncertainty integration is that of solving the OCP introduced in the previous section to obtain the distributions associated with the nominal solution ΔV_{nom}, both in terms of control effort, $\mathcal{N}(\Delta V^*, \Sigma_{\Delta V^*})$, and initial state, $\mathcal{N}(\mathbf{x_0}, \Sigma_{\mathbf{x_0}})$. Then, the initial state related to the nominal solution is taken as reference $\mathbf{x}_{0,ref}$ and propagated using a ballistic dynamical model, free from additional accelerations, from the initial t_0 to the final t_f time. Once the two states $\mathbf{x}_{0,ref}$ and $\mathbf{x}_{f,ref}$ are retrieved, the corresponding attributables are computed. This information is used to solve the OCP again on the ballistic trajectory, taking into account the same uncertainty on the BCs as before, to compute an approximate background expense related only to the uncertain BCs, $\mathcal{N}_0(\Delta V_b, \Sigma_{\Delta V_b})$.

To assess consistency of the ballistic hypothesis between the two UCTs, ΔV_{nom}, $\mathcal{N}(\mathbf{x_0}, \Sigma_{\mathbf{x_0}})$, $\mathcal{N}(\Delta V^*, \Sigma_{\Delta V^*})$ and $\mathcal{N}_0(\Delta V_b, \Sigma_{\Delta V_b})$ are used in a structured three-level screening, process that employs two statistical metrics.
The first metric leverages a figure of merit widely employed in the field of probabilistic data association, the Squared Mahalanobis Distance (SMD), that is defined as:

$$\mathrm{SMD}(\mathbf{x}) = (\mathbf{x} - \overline{\mathbf{x}})^T(\boldsymbol{\Sigma}_{\mathbf{x}} + \boldsymbol{\Sigma}_{\overline{\boldsymbol{x}}})^{-1}(\mathbf{x} - \overline{\mathbf{x}}) \sim \chi^2(\mathbf{x})\ , \tag{6}$$

DOI: 10.13009/EUCASS2025-594

where $\bar{\mathbf{x}}$ is a reference distribution mean value with associated covariance $\mathbf{\Sigma}_{\bar{\boldsymbol{x}}}$, $\mathbf{x}$ represents a sample distribution mean value with covariance $\mathbf{\Sigma}_{\boldsymbol{x}}$, and it is assumed that $(\mathbf{x} - \bar{\mathbf{x}}) \sim \mathcal{N}(\mathbf{0}, \mathbf{\Sigma}_{\boldsymbol{x}} + \mathbf{\Sigma}_{\bar{\boldsymbol{x}}})$. SMD(x) can be directly compared with a n-variable $\chi^2_{n,c}$ distribution quantifying its distance through a predefined confidence level c, related to a 3σ factor distance from its mean, leading to the definition of the correlation index $P_{SMD} = \text{SMD}(x)/\chi^2_{n,c}$.[11]

This metric is leveraged in the first verification level to test the association between the derived initial state $\mathbf{x_0}$ and the measurements composing the second track, from which the attributable $\mathbf{a_f}$ corresponding to the problem final BC is obtained. The initial state distribution $\mathcal{N}(\mathbf{x_0}, \Sigma_{\mathbf{x_0}})$ is propagated ballistically to the epochs of the second set of observations, projected onto the measurement space, and then compared with the actual measurements. This test provides an initial indication of consistency, but it is not sufficient on its own to confirm the ballistic hypothesis. Indeed, the presence of a low-thrust manoeuvre, such as a station-keeping one, may produce deviations that are not readily distinguishable from pure ballistic propagation, unless a sufficiently long time interval has elapsed to allow the divergence to become detectable.

The second level of verification instead focuses on assessing whether the nominal expense ΔV_{nom} can be explained by the ballistic background distribution. To verify this, one possible approach is considering ΔV_{nom} as a deterministic value and test it against $\mathcal{N}_0$ through a Z-score metric.
The Z-score is a statistical measure that quantifies the distance between a data point x and the mean of a dataset μ in terms of standard deviations:

$$z = \frac{x - \mu}{\sigma} \ . \tag{7}$$

To determine the probability that x lies within a certain range of the distribution, the cumulative distribution function (CDF) of the standard normal distribution Z, is used. Therefore the probability that a sample X of the distribution is going to be higher than the value of x, meaning that x is contained in the distribution itself is computed as:

$$\mathcal{P}(X \geq x) = 1 - \mathcal{P}(X \leq x) \ . \tag{8}$$

To be conservative, the threshold probability to consider the nominal expense ΔV_{nom} explained by $\mathcal{N}_0$ is set to 50%.

To enhance robustness against false positive manoeuvres, a third additional verification step is performed. By once again leveraging the SMD, it is possible to assess the correlation between the nominal distribution $\mathcal{N}(\Delta V^*, \Sigma_{\Delta V^*})$ and the ballistic background distribution $\mathcal{N}(\Delta V_b, \Sigma_{\Delta V_b})$ of expense introducing a further index referred as $P_{SMD}(\Delta V)$. For all the analyses carried out, due to the low orders of magnitude of the involved variable, the logarithm of the expense is employed to avoid incurring in numerical errors, as suggested in Serra.[13]

To improve the accuracy of nonlinear uncertainty propagation, a 4th-order Conjugate Unscented Transform (CUT4) is employed instead of the UT. While the UT captures the first two moments of a Gaussian distribution exactly and offers third-order accuracy for symmetric functions, it may fail to represent higher-order statistical features when the system dynamics are highly nonlinear, as is often the case in cislunar orbital mechanics. The CUT4 extends the accuracy to fourth-order moments, enabling a more faithful approximation of transformed distributions when compared to Monte Carlo references, especially in terms of shape, tail behavior, and variance structure.[1] An initial assessment of the suitability of the CUT4 approach is performed by directly comparing its results to those obtained through Monte Carlo simulation. Despite the higher number of sigma points required due to the problem dimensionality, CUT4 remains significantly more computationally efficient than a Monte Carlo approach.

3. Simulations and results

This section presents the results of the conducted simulations. The two scenarios involved are distinguished by the observer location. In the first case, measurements are acquired from a ground-based sensor, specifically the French TAROT Calern station. In the second scenario, a space-based sensor positioned in a Halo orbit around the L1 Lagrange point is considered.

3.1 Ground-based

For the ground-based case, the first step involved acquiring measurements of the target. The analysis considered two representative orbits belonging to the Lyapunov and Halo families around the L1 point. A visibility analysis, accounting for the major observational constraints, is performed to derive the corresponding visibility windows and, consequently, to retrieve the objects observation tracks.

For this analysis, the observation time span is set equal to the orbital period of the relative targets being 14.44 days for the Lyapunov-L1 and 11.42 days for the Halo-L1. The visibility windows for the two candidate orbits are shown in

DOI: 10.13009/EUCASS2025-594

Fig. 2 and Fig. 3, respectively. The sensor accuracy is taken as standard deviation of the angular measurements acquired, traducing in an attributable standard deviation of the order of $\sigma_{\mathbf{a}} = [1e{-}06 \text{ rad}, \ 1e{-}06\text{rad}, \ 1e{-}09 \text{ rad/s}, \ 1e{-}09 \text{ rad/s}]$.

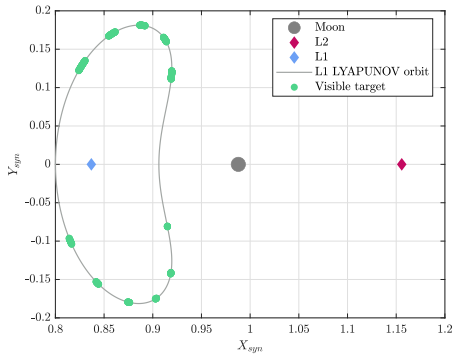

Figure 2: L1 Lyapunov orbit visibility.

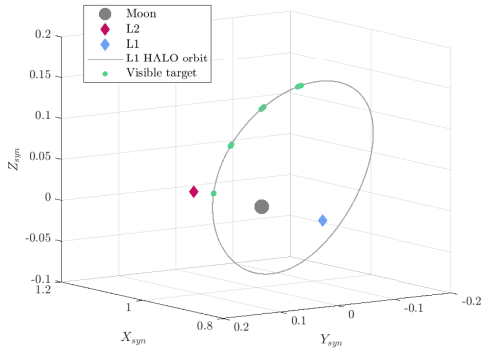

Figure 3: L1 Halo orbit visibility.

Once the measurements are retrieved, optical UCTs are constructed by selecting one measurement set per hour within the visibility window. For the simulation setup, the attributable $\mathbf{a_0}$ corresponding to the first track is computed and used as the initial BC for the OCP. The final BC is then varied by selecting subsequent tracks. To maintain a consistent basis for comparison between the two orbital regimes, the maximum time separation Δt_{UCTs} between the first and subsequent tracks is set to 5 days for the Lyapunov-L1 case. This choice is motivated by the fact that, in the Halo-L1 scenario, the maximum available separation is approximately 3 days, thus, setting a similar time frame allows, for a meaningful comparison of the results in the two different scenarios.

As first assessment, the hypothesis on the normality of the expense distribution is performed. The reference case considered takes into account the maximum Δt_{UCTs} between consecutive observations, that is 5 days for the Lyapunov case. A Kolmogorov-Smirnov test is performed on the expense distribution retrieved from a Monte Carlo simulation, accounting for 500 samples, to validate the hypothesis of normality at a significance level of 5%. The comparison between the empirical CDF and the equivalent standard normal is reported in Fig. 4(a), it is evident that the distribution does not hold the normality hypothesis. Moreover, in Fig. 4(b) the quantiles of the two distributions are reported to better appreciate the divergence which affects in particular the tails of the Monte Carlo distribution. Nonetheless, a further test to assess how inaccurate would be to approximate the distribution using only its first two moments is performed. By comparing the CDFs obtained from the Monte Carlo simulation and the CUT4 method, it is evident from Fig. 4(c) that, although the Monte Carlo distribution is not strictly Gaussian, the first two moments, mean and covariance, are nonetheless well captured by the CUT4 model. Hence, this approach serves as a valid and reasonably representative alternative to characterise the distribution.

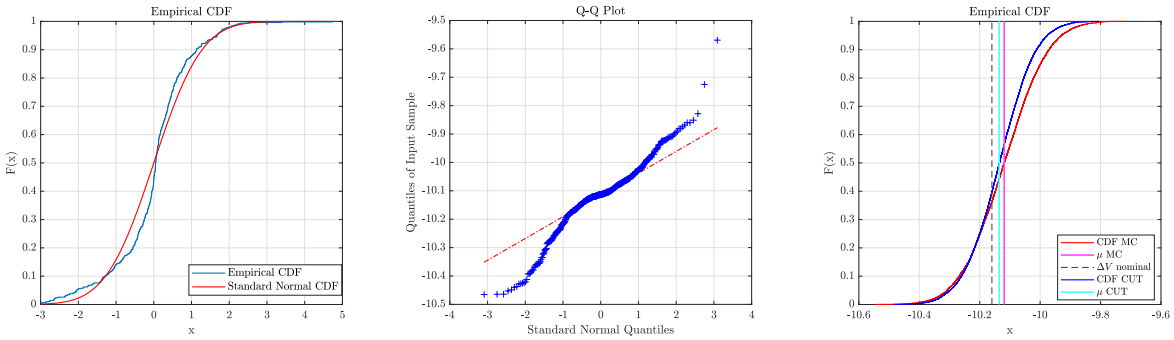

(a) (b) (c)

Figure 4: Plot (a) reports the Kolmogorov-Smirnov test performed on the Monte Carlo ΔV_b distribution. Plot (b) shows the trend of the distribution quantiles with respect to the normal quantiles. Plot (c) includes the comparison between the CUT4 and the Monte Carlo approach on the ΔV_b distribution. All the graphs are referred to the last Lyapunov-L1 UCT pair (highest Δt_{UCTs}).

Regarding the results of the three levels of verification applied to the ballistic hypothesis for the two orbital test cases considered, these are presented in Fig. 5. Specifically, Fig. 5(a) reports the outcomes of the correlation index

DOI: 10.13009/EUCASS2025-594

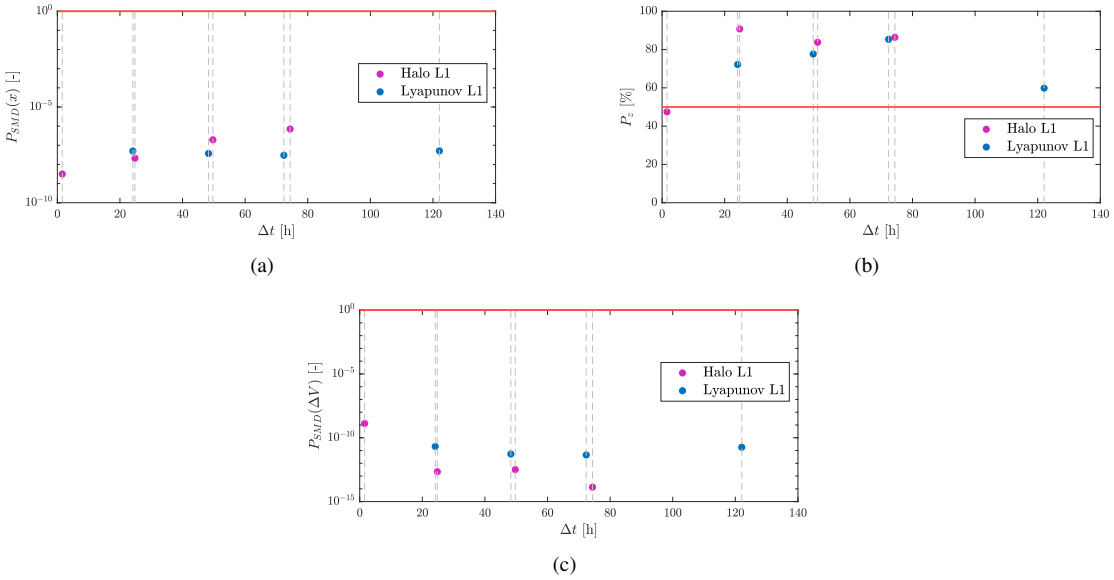

Figure 5: Plot (a) reports the outcomes of the first step based on $P_{SMD}(x)$. Plot (b) shows the probability P_z linked to the second Z-score-based step. Plot (c) includes the values of $P_{SMD}(\Delta V)$ resulting from the third step. The graphs include both candidates orbits.

$P_{SMD}(x)$, computed over the distribution of the initial state associated with the nominal resolution of the OCP. In all the analyzed cases, this first level of control yields positive results, immediately ruling out the possibility that the two tracks are connected by an high-thrust manoeuvre.
After the first verification level is satisfied, the method proceeds to examine whether the ΔV_{nom} is consistent with the ballistic distribution, based on a Z-score analysis. The results shown in Fig. 5(b) highlight that, in the majority of cases, the expense values are inherently consistent with the ballistic distribution, even when adopting a conservative threshold of 50%. However, it may occur, such as in the first Halo-L1 case, that the probability falls below the threshold.
To verify whether this outcome indeed indicates the presence of a low-thrust manoeuvre, the third level of verification is introduced. This last check leverages the additional SMD-based index, assessing the correlation between the two expense distributions, the corresponding $P_{SMD}(\Delta V)$ values are reported in Fig. 5(c). Although this control is mainly designed for cases that do not satisfy the Z-score criterion, for completeness and to enable comparison across all cases, the indices have been computed for every pair of tracks. Notably, the $P_{SMD}(\Delta V)$ value associated with the previously highlighted case, remains within the expected bounds and is consistent with the other scenarios analyzed.
Therefore, it can be concluded that in none of the cases considered does the expense distribution resulting from the OCP resolution appear anomalous compared to a ballistic distribution driven solely by uncertainties in the BCs.

3.2 Space-based

The space-based scenario involves an observer positioned on the same Halo-L1 orbit described in the previous case and a target located on a reference Distant Retrograde Orbit (DRO).

As in the previous case, a relative visibility analysis between the two objects is conducted, including the additional observability constraints specific to the space-based configuration.
The temporal span of the analysis is set equal to the longest of the two orbital periods. In this case, it corresponds to the observer period, since the target one is of approximately 7 days.
For the on-board optical sensor, a reference angular accuracy of 1 arcsecond, in both α and δ, is assumed. This results in an attributable standard deviation of the order of $\sigma_{\mathbf{a}} = [1e-06 \text{ rad},\ 1e-06 \text{rad},\ 1e-08 \text{ rad/s},\ 1e-08 \text{ rad/s}]$.
The analysis produced a visibility window, depicted in Fig. 6, of approximately 18 hours between the two objects which is relatively short compared to the total analysis duration of 14.44 days. As in the ground-based test case, one track is generated for each hour of visibility, resulting in a total of 18 UCTs. Among these a subset is selected, containing those tracks having a $\Delta t = [3, 7, 9, 13, 17]$ hours approximately, with respect to the first one. Rather than selecting all samples, which would be closely spaced in time, this subset is chosen to span the full temporal scale between the first and the last sample. This allows for a more representative analysis of the effect of Δt_{UCTs} over the entire observation window. The first UCT within the visibility window is used to extract the attributable $\mathbf{a_0}$ corresponding to the initial

DOI: 10.13009/EUCASS2025-594

BC. This is then tested against each of the subsequent 5 tracks, from which the final attributable BC $\mathbf{a_f}$ is derived, as a function of time.

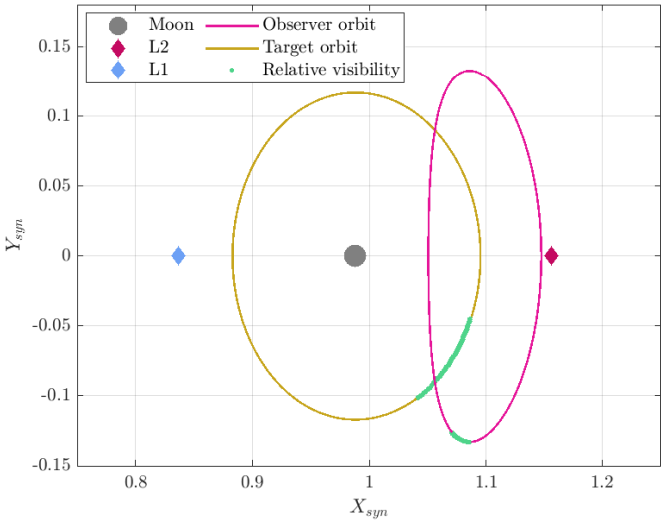

Figure 6: Relative visibility between observer (Halo-L1) and target (DRO).

Once again, the fidelity of the CUT4 model in replicating the Monte Carlo distribution is assessed. This verification aims to evaluate any discrepancies with respect to the previous case that may arise due to the different sensor accuracy. Also in this case, the expense distribution does not pass the Kolmogorov-Smirnov test, as it can be graphically appreciated in Fig. 7(a). From Fig. 7(b) it can be seen the deviation of the quantiles along both tails, less pronounced than that of the previous test case but still dominant. In the same way as before, the CDFs of the CUT4 approach and the Monte Carlo are computed and compared in Fig. 7(c). Also in this case the fist two moments of the distribution coincide, so it is reasonable, for this second test case as well, leveraging the CUT4 approach.

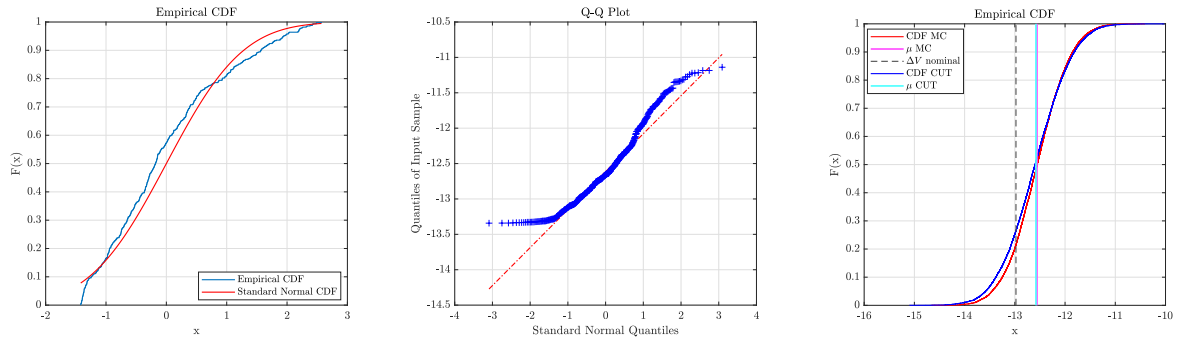

(a) (b) (c)

Figure 7: Plot (a) reports the Kolmogorov-Smirnov test performed on the Monte Carlo ΔV_b distribution. Plot (b) shows the trend of the distribution quantiles with respect to the normal quantiles. Plot (c) includes the comparison between the CUT4 and the Monte Carlo approach on the ΔV_b distribution. All the graphs are referred to the last UCT pair (highest Δt_{UCTs}).

As in the previous test case, the three-step verification framework is used to evaluate the ballistic hypothesis, and the outcomes are shown in Fig. 8. The values corresponding to the first verification level on $P_{SMD}(x)$ are reported in Fig. 8(a). Consistent with earlier findings, this initial check yields positive results across all attributable pairs, ruling out the possibility of high-thrust manoeuvres as the source of the observed motion.
The second step based on the Z-score is then carried out and the respective results are presented in Fig. 8(b). In most cases, the nominal expense falls within the expected range, considering the conservative 50% probability threshold. However, similar to the ground-based case, outliers may emerge and for this test case the computed likelihood dips below the threshold twice, indicating a potential deviation from pure ballistic dynamics.

DOI: 10.13009/EUCASS2025-594

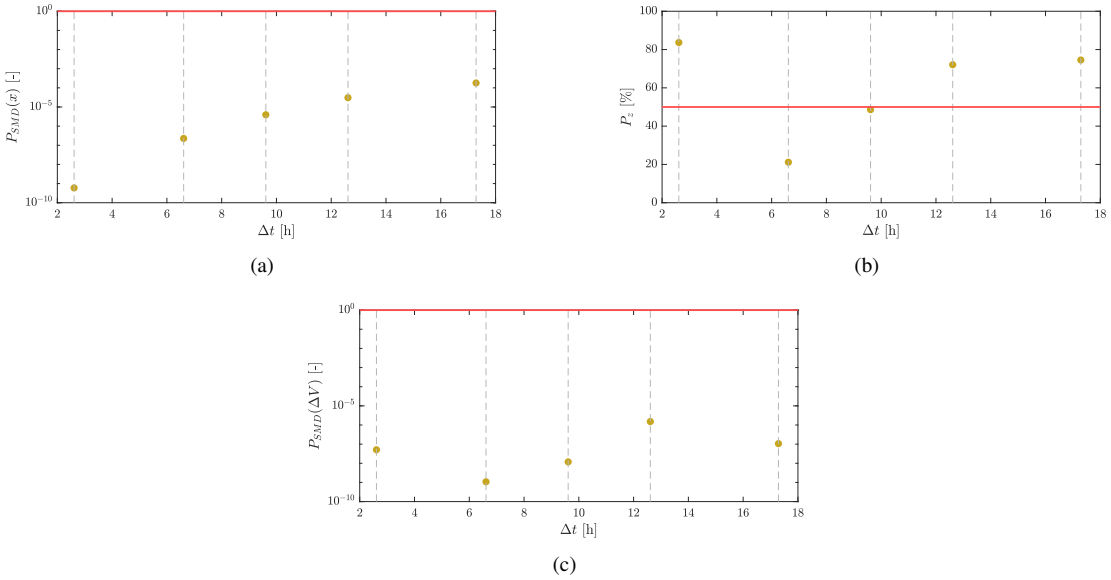

Figure 8: Plot (a) reports the outcomes of the first step based on $P_{SMD}(x)$. Plot (b) shows the probability P_z linked to the second Z-score-based step. Plot (c) includes the values of $P_{SMD}(\Delta V)$ resulting from the third step. The graphs are related to the target DRO object.

To further investigate such cases, the third step is triggered to evaluate $P_{SMD}(\Delta V)$ between the computed expenses, the resulting values are shown in Fig. 8(c). Also for this case $P_{SMD}(\Delta V)$ it is computed for all UCT pairs to provide a complete comparison across the dataset. In the case identified by the Z-score as potentially non-ballistic, the $P_{SMD}(\Delta V)$ value nonetheless aligns with those observed in fully consistent cases.

As in the previously analyzed scenario, this reinforces the conclusion that the apparent deviation does not reflect a genuine manoeuvre but remains statistically compatible with the uncertainty BCs derived background distribution.

4. Conclusions

This work has presented the application of a correlation technique based on the solution of a minimum-energy optimal control problem between two optical UCTs associated with objects operating in the cislunar regime.

The focus was set on testing the ballistic dynamics hypothesis to correlate two UCTs by comparing the OCP-derived control expense, both as a deterministic value and as a distribution, with an approximate background distribution linked to the BCs uncertainty. The use of transversality conditions simplifies the problem by removing the need to define an admissible region and by relaxing assumptions about the underlying dynamics.

The proposed method was evaluated through test cases involving both ground-based and space-based optical measurements, covering a representative range of observation scenarios relevant to future operational contexts in cislunar space. The results of the three-step verification framework for assessing the ballistic hypothesis showed consistent positive outcomes across all of the analysed cases. These findings support the validity of the method in identifying dynamical consistency between UCT pairs.

Future work will include sensitivity analyses to evaluate the impact of both varying levels of measurement and initial IOD guess state uncertainty, on the method performance and reliability. Additionally, further studies will investigate the robustness of the approach with respect to the adopted dynamical model, for instance by using a full ephemeris model for measurement generation and propagation.

5. Acknowledgments

This research has received funding as part of the work developed for the agreement n. 2023-37-HH.0 for the project "Attività tecnico-scientifiche di supporto a C-SSA/ISOC e simulazione di architetture di sensori per SST", established between the Italian Space Agency (ASI) and Politecnico di Milano (POLIMI). The contributions of Mrs. De Riz have been made possible thanks to funding from the European Union – NextGenerationEU, under Mission 4, Component 1 (CUP: D43C22002780001), whose support is gratefully acknowledged.

DOI: 10.13009/EUCASS2025-594

References

[1] N. Adurthi, P. Singla, and T. Singh. The conjugate unscented transform—an approach to evaluate multi-dimensional expectation integrals. In *2012 American Control Conference (ACC)*, pages 5556–5561. IEEE, 2012.

[2] M. Bolden, I. Hussein, H. Borowski, R. See, and E. Griggs. Probabilistic initial orbit determination and object tracking in cislunar space using optical sensors. In *Advanced Maui Optical and Space Surveillance Technologies (AMOS) Conference*, pages 27–30, 2022.

[3] A De Riz, R Cipollone, P Di Lizia, et al. Optimal control-based track-to-track correlation with optical measurements. In *Advanced Maui Optical and Space Surveillance (AMOS) Technologies Conference*, pages 1–10, 2024.

[4] G. F. Gronchi, L. Dimare, and A. Milani. Orbit determination with the two-body integrals. *Celestial Mechanics and Dynamical Astronomy*, 107:299–318, 2010.

[5] M. J. Holzinger, D. J. Scheeres, and K. T. Alfriend. Object correlation, maneuver detection, and characterization using control distance metrics. *Journal of Guidance, Control, and Dynamics*, 35(4):1312–1325, 2012.

[6] IADC. Iadc space debris mitigation guidelines. Technical report, Inter-Agency Space Debris Coordination Committee, 2020.

[7] X. Liu, R. Armellin, L. Pirovano, and X. Hou. Initial orbit determination of periodic orbits in the earth–moon system with ground-based optical observations. *IEEE Transactions on Aerospace and Electronic Systems*, 60(6):8992–9005, 2024.

[8] X. Liu, X. Hou, and R. Armellin. Multiple solutions of initial orbit determination in cislunar space. *Advances in Space Research*, 2025.

[9] A. Milani, M. E. Sansaturio, and S. R. Chesley. The asteroid identification problem iv: Attributions. *Icarus*, 151(2):150–159, 2001.

[10] A. Pastor, G. Escribano, and D. Escobar. Satellite maneuver detection with optical survey observations. In *Advanced Maui Optical and Space Surveillance Technologies Conference (AMOS)*, 2020.

[11] L. Pirovano, R. Armellin, J. Siminski, and T. Flohrer. Differential algebra enabled multi-target tracking for too-short arcs. *Acta Astronautica*, 182:310–324, 2021.

[12] A. Scorsoglio, A. D'Ambrosio, L. Ghilardi, R. Furfaro, and V. Reddy. Physics-informed orbit determination for cislunar space applications. In *Proceedings of the Advanced Maui Optical and Space Surveillance (AMOS) Technologies Conference*, page 1, 2023.

[13] R. Serra, C. Yanez, and C. Frueh. Tracklet-to-orbit association for maneuvering space objects using optimal control theory. *Acta Astronautica*, 181:271–281, 2021.

[14] J. Siminski, H. Fiedler, and T. Flohrer. Correlation of observations and orbit recovery considering maneuvers. *AAS/AIAA Space Flight Mechanics*, 2017.

[15] S. Wishnek, M. J. Holzinger, and P. Handley. Robust cislunar initial orbit determination. In *AMOS Conf. Proc*, 2021.